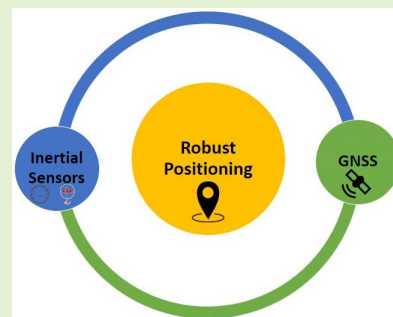# Robust Positioning for Road Information Services in Challenging Environments

Amr S. El-Wakeel, *Student Member, IEEE*, Abdalla Osman, *Member, IEEE*,
Nizar Zorba, *Senior Member, IEEE*, Hossam S. Hassanein, *Fellow, IEEE*,
and Aboelmagd Noureldin, *Senior Member, IEEE*

Abstract—Next-generation Intelligent Transportation Systems (ITS) of future road traffic monitoring will be required to provide reports on traffic status, road conditions, and driver behaviour. Road surface anomalies contribute to increasing the risk of traffic accidents, reduced driver comfort and increased vehicles' damage. The conventional integrated Global Navigation Satellite System (GNSS)/ Inertial Navigation System (INS) positioning solutions can suffer from errors because of inertial sensor noises and biases, especially when low-cost and commercial grade inertial sensors are used. In this work, we use a reduced inertial sensor system utilizing Micro-Electro-Mechanical-System (MEMS) based inertial sensors, to integrate with the GNSS receiver and provide robust positioning in urban canyons. To provide acceptable performance in challenging urban environments, our method de-noises the MEMS-based inertial sensor measurements using a technique based on a Bi-orthonormal search, which separates the monitored motion dynamics from both the inertial sensor bias errors and high-frequency noises. As a result, the performance of the positioning system is improved, providing reliable positioning accuracy during extended GNSS outages that occur in various areas. To show the significant enhancement achieved by the proposed approach, we examined the system performance over three road test trajectories involving MEMS-based inertial sensors and GNSS receivers mounted on our test vehicle. The superior performance of our proposed INS/GNSS integrated positioning system is demonstrated in this paper during various GNSS outages, in different areas, and under multiple driving scenarios.

Index Terms— Road information services, intelligent transportation systems, connected vehicles, positioning, spectral de-noising, Kalman filter.

A. S. El-Wakeel is with the Department of Electrical and Computer Engineering, Queen's University, Kingston, ON K7L 3N6, Canada (e-mail: amr.elwakeel@queensu.ca).

A. Osman is with the Department of Electrical and Computer Engineering, Royal Military College of Canada, Kingston, ON K7K 7B4, Canada (e-mail: abdalla.osman@rmc.ca).

N. Zorba is with the Department of Electrical Engineering, Qatar University, Doha, Qatar (e-mail: nizarz@qu.edu.qa).

H. S. Hassanein is with the School of Computing, Queen's University, Kingston, ON K7L 2N8, Canada (e-mail: hossam@cs.queensu.ca).

A. Noureldin is with the Department of Electrical and Computer Engineering, Royal Military College of Canada, Kingston, ON K7K 7B4, Canada, with the School of Computing, Queen's University, Kingston, ON K7L 2N8, Canada, and also with the Department of Electrical and Computer Engineering, Queen's University, Kingston, ON K7L 3N6, Canada (e-mail: aboelmagd.noureldin@rmc.ca).

Digital Object Identifier 10.1109/JSEN.2019.2958791

I. INTRODUCTION

A. Background and Motivation

SMART cities' are receiving tremendous interest from governments and the demands, challenges, and applications are the primary focus of the Information and Communication Technology (ICT) community. According to the consume news and business channel (CNBC) [1], various cities around the world are expected to invest $41 trillion in smart technologies within the next two decades.

Furthermore, in their report regarding the Smart City challenge, the U.S. Department of Transportation has assessed the effect of smart technologies in ITS on the development of smart cities [2]. The rapid evolution of sensing technologies led to a broad acceptance and wide range of applications of ITS and Road Information Services (RIS) [3], [4]. Consequently, ITS and RIS contribute dramatically towards the advancement of future smart cities [5], [6]. Recently, there have been numerous applications on the evolvement of intelligent vehicles, including driver behaviour assessment and safety-related issues regarding the occupants of the vehicle [7], [8]. While in [9]–[12], the authors used

crowdsourcing for RIS, traffic management, and road surface conditions monitoring.

Undoubtedly, robust positioning and localization-based systems are required for ITS and RIS systems and applications to perform efficiently [13], [14]. Specifically, monitoring road surface anomalies such as potholes and utility holes requires adequate positioning for the monitored events [12], [15]. Otherwise, the detection of these events can be misleading or useless. To date, GNSS receivers are the most popular candidate for location determination, but this technology faces a few challenges which limit its capabilities [14]. Severe multipath and total signal blockage in downtown cores and urban areas are the significant challenges in acquiring accurate and continuous geo-referencing [13].

To overcome GNSS positioning systems challenges, INS, when integrated with GNSS receivers, provides accurate and continuous positioning [14]. Low-cost MEMS-based inertial sensors (accelerometers and gyroscopes) that are embedded in INS systems in land-vehicles and ubiquitous smart devices are not susceptible to the same challenges of GNSS. However, stand-alone INS solutions are prone to long-term position drifts and errors [16]. To avoid positioning errors in INS solutions, inertial sensors' biases and different sources of noises were analyzed and assessed. In particular, inertial sensors noises were categorized into short and long-term errors [17], [18]. The short-term errors are dominated by high-frequency components, while long-term errors are presented by low-frequency components. Short term errors (i.e., additive white Gaussian noise) are a result of electronic equipment and power supplies. Also, the random angle walk is considered short-term noise due to its high-frequency nature [18].

On the contrary, exponentially correlated noise that results from internal or external temperature variations is considered as long-term errors [17]. Bias instability from electronic components appear in low-frequency components and is also regarded as long-term errors [18]. To suppress inertial sensor noises, in [19], a Wavelet Multi-Resolution Analysis (WMRA) was proposed to eliminate the long-term errors of INS that are mixed with low frequencies, to describe the vehicle motion. WMRA adopted a wavelet function of the Daubechies family together with a soft thresholding technique. However, the lack of sufficient experimental results that span different and complicated real driving scenarios limit the reliability of the proposed method.

Authors in [20], applied a Daubechies wavelet-based de-noising technique to eliminate inertial sensor noise before integrating INS with GNSS in a combined solution. The proposed method used soft thresholding for noise-suppressing, and the authors compared their integration system after de-noising with low pass filtering (LPF) - based system integration. The results did not show significant enhancement regarding root mean square error, as the wavelet-based integrated system outperforms the LPF by approximately 20%. Also, the major limitation of the authors' proposed scheme is that they only considered GNSS without INS. In [21], a de-noising technique that combines wavelet de-noising and Allan Variance (AV) analysis was proposed to suppress both short and long-term noises. The authors utilized road test experiments to assess the proposed de-noising technique on the performance of loosely coupled INS/GNSS integration. In their results, the combined de-noising method achieved a maximum error of 53.61 m compared to 92.51 m obtained by AV de-nosing only. The major drawback is that AV needs big data sets to produce consistent AV curves, which introduces additional complexity to the proposed solution. Also, the lack of experimental validation with extended and multiple GPS outages made the assessment of the positioning error enhancement not clear enough.

In [22], a high-resolution spectral analysis algorithm named Fast Orthogonal Search (FOS) was adopted. FOS models the low-frequency band that contains the vehicle dynamics to suppress short and long-term errors of the inertial sensors. The main advantage of FOS is in adopting a non-orthogonal candidate function that is capable of determining a frequency component between the Fast Fourier Transform (FFT) bins. This technique avoids the energy dissemination into other integer frequency component, which is known by spectral leakage phenomena [23]. The FOS algorithm divided the data into small windows to assume stationarity at each time window. One limitation in [22] is that the maximum tackled outage length was 40 seconds. This outage period is not reflecting complicated scenarios such as downtown cores that can experience a few minutes of continuous GNSS outages.

Considering INS/GNSS integrated positioning systems, there are various integration approaches that entirely or partially utilize the Inertial Measurement Units (IMUs) as embedded accelerometers and gyroscopes [14], [24], [25]. Applying the Kalman Filter (KF) in the integration of GNSS and INS was the most utilized integration methodology [14], [15]. On the other hand, the Particle Filter (PF) was proposed as a competitive alternative for integrated positioning [26], [27]. Consequently, the major challenge of the linearized KF is that the stochastic sensor errors and navigation error states are linearly modelled. Such linearized modelling leads to solution divergence, especially during GNSS extended outages [24].

On the other hand, PF techniques such as Sampling/ Importance Re-sampling (SIR), Mixture PF (MPF) and Parallel Cascade Identification PF (PCI PF) have the capabilities of nonlinear modelling [27], [28]; that allow the PF to model high order motion dynamics and noise characteristics [14]. The major challenge in adopting PF techniques for INS/GNSS integration is their high computational complexity compared to the linearized KF and extended Kalman filter (EKF) [14].

Also, during extended GNSS outages, the integration solutions mainly rely on the full inertial measurement units (IMUs), which have limitations due to the uncompensated biases [14]. The integration filters are operated in prediction mode when the GNSS updates are not available. The predicted INS errors are being considered in the mechanization solution to enhance its performance. However, the compensation is not always efficient, and notable residual errors are remaining [14], [16]. A Reduced Inertial Sensor System (RISS) [14] is utilized to overcome the INS biases and noise errors.

In RISS, only two accelerometers, one gyroscope and a wheel odometer, are used instead of full IMUs. The odometer speed is considered in RISS to avoid the errors of the accelerometer biases. The pitch and roll angles are computed through combining accelerometers and odometer measurements, thus to prevent the horizontal gyroscope errors and biases [14]. Nevertheless, noise from inertial sensors and errors need to be eliminated to enhance the performance of the RISS in extended GNSS outages.

B. Problem Statement

As previously mentioned, obtaining an accurate and continuous positioning is challenging when only relying on GNSS receivers in urban areas and downtown cores. Also, the solution of adopting inertial sensors embedded in INS for providing an integrated positioning solution along with GNSS has two main challenges: the first one is the inertial sensor noise that leads to high drifts and errors in the positioning solution, especially during GNSS outages. The second one is the error from using linearized integration filters or the demanding computational complexity of the non-linear integration filters.

Accordingly, to maintain a robust and consistent ITS for RIS applications, a reliable and continuous positioning system should be adopted to overcome the previously mentioned challenges.

C. Contribution

The specific contributions of this paper are in the field of INS/GNSS integration and are the following:

a- Proposing a Bi-Orthonormal (BIO) technique for de-noising raw measurements, being used on the low-cost MEMS accelerometers and gyroscopes that are employed for INS in the 3D RISS.

b- Enabling the operation of the 3D RISS system independently over various periods without GNSS measurements, both in downtown areas and other GNSS denied environments.

c- Demonstrating the performance of the proposed BIO-enabled 3D RISS through road test experiments in downtown Kingston, ON, and Montreal, QC. We also compare the performance to the recently published methods in the same areas.

II. METHODOLOGY

In this section, we present the system configuration used to integrate INS/GNSS to provide a 3D (longitude, latitude and altitude) navigation solution. Generally, INS/GNSS is incorporated into different forms and techniques. Regarding the integration forms, a full IMU with six degrees of freedom (three accelerometers and three gyroscopes) is used to provide the INS solution and then is integrated with GNSS [27], [28]. Partial usage of the IMU is applied to provide INS/GNSS in [14], [29] to eliminate the effects of the sensor errors. In RISS, a single gyroscope with its sensitive axis coincides with the vertical axis of the land vehicle, the forward and transverse accelerometers, which, together with an odometer, are all used to provide the INS solution [14], [30].
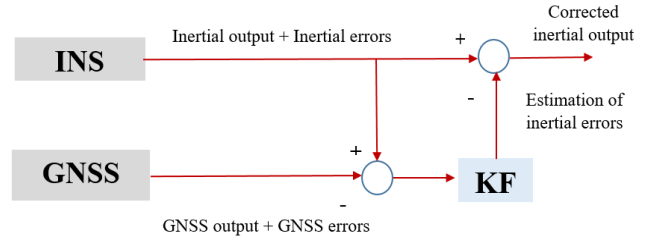

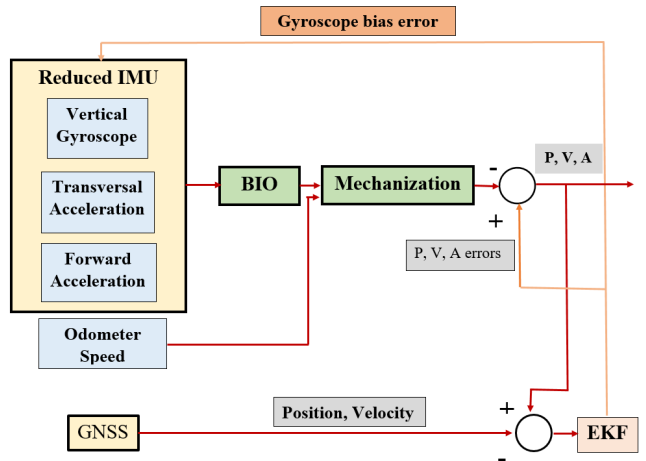Fig. 1. System model of INS/GNSS KF integration.

Fig. 2. EKF-Based BIO-3D RISS/GNSS closed-loop loosely coupled integrated positioning system, where P, V and A are the position velocity and attitude, respectively.

The integration techniques are provided by either linearized estimation filters (e.g., KF and EKF), or nonlinear filters (e.g., PF) [14], [26], [27], [30]. Another classification can be done with regards to the GNSS/INS coupling tightness, where the setups are loosely coupled, tightly coupled, or ultra-tightly coupled integration [14], [29].

A. System Model

For the INS/GNSS integration, INS increasingly drifts with time due to the implicit mathematical combination within the mechanization process, which causes the bias errors of both accelerometers and gyroscopes to be accumulated [21]. KF can be utilized in INS to optimally estimate the error-state, including position errors, velocity errors and orientation errors. In general, KF is an algorithm for optimally estimating the error state of a system from measurements corrupted by noise. The KF algorithm is a sequential recursive algorithm for optimal least-mean variance estimation of the error states. In addition to its benefits as an optimal estimator, the KF provides real-time statistical data related to the estimation accuracy of the error states. This data is very useful for quantitative error analysis [14]. In Figure 1, we present the system model used for INS/GNSS integration.

As shown in Figure 2., within this paper, we adopt a closed-loop 3D RISS loosely coupled integration because it is robust and simple to implement compared to the other integration forms [14]. In the following subsections, we present in detail

the BIO-based signal de-noised 3D RISS/GNSS positioning system.

B. Bi-Orthonormal De-Noising Technique

As mentioned earlier, a powerful de-noising for the inertial sensors is required to suppress the short and long-term noises. In literature, there were multiple spectral analysis techniques used for signal representation and de-noising such as FFT [20], Short Windowed Fourier Transform (SWFT) [14], Wavelet-based Multi-Resolution Analysis (WMRA) [19] and FOS [22]. All these proposed techniques have limitations in de-noising the inertial sensors at low and high frequencies.

We propose to use the BIO technique to provide the required de-noising for our setup, as it will reduce the dimensions required to represent any vector, and thus, it decreases the noise impact. The proposed method employs optimized selection criteria to determine candidate functions (basis). This basis represents the outputs of the sensors using an over-complete dictionary of candidate functions and finally compute their corresponding coefficients. Hence BIO offers a significant enhancement for sensor output analysis and reconstruction accuracy.

The BIO optimal signal representation [31], [32] is based on defining a k-dimensional subspace H_1 of a Hilbert space, H spanned by a set of basis $\{l_i\}$. Then, the subspace H_1 is a k-dimensional subspace spanned by a partial set of basis $\{l_1, l_2, \ldots, l_k\}$. The optimal bi-orthogonal technique generates two sets of bi-orthonormal basis linked to the partial set of basis. The first set is the bi-orthonormal set $\{h_1, h_2, \ldots, h_k\}$ that is related to the partial set of basis in H. The second one is $\{\hat{h}_1, \hat{h}_2, \ldots, \hat{h}_k\}$ that is linked to the same partial set of basis in H_1.

For a vector y that belongs to H, the closest vector to y in the minimal norm sense from amongst the vectors in H_1, is defined by $\hat{y} = \sum_{i=1}^{k} \langle y, \hat{h}i \rangle l_i$. The main idea is to find the closest vector $\hat{y}$ to y while being represented in a lower number of dimensions. Considering the theorem of bi-orthonormal optimal approximation [31], the optimal approximation coefficients of vector y belonging to H through subspace H_1 are the projections of y on vectors $\{\hat{h}_1, \hat{h}_2, \ldots, \hat{h}_k\}$ which are bi-orthonormal to the given partial set $\{l_1, l_2, \ldots, l_k\}$ spanning H_1, and belonging to H_1.

The bi-orthonormal set $\{\hat{h}_1, \hat{h}_2, \ldots, \hat{h}_k\}$ related to a finite set of basis $\{l_1, l_2, \ldots, l_k\}$ belonging to the space spanned by the given basis, is calculated through the following steps:

a. Establishing the inner product matrix between the basis $\{l_1, l_2, \ldots, l_k\}$ elements to give a matrix of scalars P_X:

$$P_x \triangleq \begin{bmatrix} \langle l_1 l_1 \rangle & \cdots & \langle l_k l_1 \rangle \\ \vdots & \cdots & \vdots \\ \langle l_1 l_k \rangle & \cdots & \langle l_k l_k \rangle \end{bmatrix} \quad (1)$$

b. Calculating the inverse matrix P_l^{-1} which represents all the inner product combinations between the elements of the bi-orthonormal set $\{h_1, h_2, \ldots, h_k\}$ associated with the basis $\{l_1, l_2, \ldots, l_k\}$ elements:

$$P_l^{-1} \triangleq \begin{bmatrix} \langle h_1 h_1 \rangle & \cdots & \langle h_k h_1 \rangle \\ \vdots & \cdots & \vdots \\ \langle h_1 l_k \rangle & \cdots & \langle h_k h_k \rangle \end{bmatrix} \quad (2)$$

c. Using the matrix P_l^{-1}, the elements of the set $\{h_1, h_2, \ldots, h_k\}$ are obtained employing the linear combination:

$$\hat{h}i = \sum_{j=1}^{k} \langle h_i h_l \rangle l_j \quad \text{For } j = 1, 2, .., k \quad (3)$$

where each one of the inner products is obtained from the matrix in Eqn. (2). These steps present an optimal approximation of signal y given that the partial set of basis $\{l_1, l_2, \ldots, l_k\}$ is already known. The elements of a partial set of basis are usually unknown and then determining the partial set of basis is crucial to the signal representation steps.

The optimum signal representation can be achieved by searching the partial representation set and selecting basis elements one at a time. The selection criterion of a term to be added to the representation depends on the minimization of the signal representation error. The error is computed through norm-2 of the difference between the original signal and the obtained representation utilizing the considered term as

$$l_m = \underbrace{min}_{m} \{\|y - y_m\|\} \quad (4)$$

where y_m is the signal vector formed by adding the mth term of the signal representation basis set. The algorithm selects a term that minimizes the error model. Subsequently, the selection of additional terms from the pool of the residual basis elements is conducted. BIO adopts three stopping conditions for the selection algorithm. The first is achieved by pre-determining the number of terms to be added to the signal approximation. While the second can be obtained through a thresholding technique where the algorithm stops adding terms if the error reduction is kept below a specific threshold. With the prior knowledge of the original signal representation, BIO stopping criterion can be applied when the error level between the constructed signal and the original one meets a sufficient threshold. This sequential procedure of signal representation requires the construction of the matrix P_x and it's inverse at each step. This is followed by the development of approximate signal representation, y_m. The number of floating-point operations, γ, required for optimum signal representation is equal to [33]:

$$\gamma = MK \left(K^3 + \frac{K^2}{2} (6N - 1) + \frac{K}{2} (10N - 1) - N \right) \quad (5)$$

where N is the number of samples in vector $\mathbf{y}$, K is the number of basis elements, and M is the number of selected basis elements. γ may increases extraordinarily by increasing the number of terms (K), length of signal (N) and the number of basis chosen elements (M). BIO reduces the algorithm processing time and complexity through averting multiple matrix computations by deriving the term selection criteria.

As shown in Figure 2, the readings of one gyroscope and two accelerometers of the RISS system are the input of the BIO stage. In the BIO stage, we applied the introduced algorithm to de-noise the gyroscope and accelerometers data to suppress both short and long-term errors and noises. The continuously de-noised linear accelerations and angular rotations will enhance the results of the mechanization process and improve the accuracy of the computed position updates through the RISS/GNSS integration module described in the following section.

C. 3D RISS/ GNSS Integration

As we stated before and shown in Figure 2, we adopted 3D RISS that utilize one gyroscope, two accelerometers and an odometer. The main advantage of using the 3D RISS rather than full IMU is when the pitch and roll angles are calculated using accelerometers. The biases or noises of the two omitted gyroscopes are avoided. Also, calculating the velocity using the forward speed gathered by the odometer allows bypassing any uncompensated noises or biases of two accelerometers [14], [26], [34]. Accordingly, the de-noised sensor signals along with the odometer measurements, are the input for the mechanization process. Basically, the navigation state vector of 3D RISS is given by $x = [\varphi, \lambda, \Omega, v_e, v_n, v_u, r, p, A]^T$ where φ is the latitude, λ is longitude, Ω is altitude, v_e is the velocity towards east, v_n is the velocity towards north, v_u is the up velocity, r is the roll angle, p is the pitch angle, and A is the azimuth. Consequently, pitch angle is given by the [32], [34]:

$$p = sin^{-1}\left(\frac{f_y - a_{od}}{g}\right) \tag{6}$$

where f_y is the forward acceleration, a_{od} is the vehicle acceleration calculated using the vehicle acceleration recorded by the odometer, and g is the gravitational acceleration. The roll angle is obtained as follows [34], [35]:

$$r = -\sin^{-1}\left(\frac{f_x + v_{od}\omega_z}{g\cos p}\right) \tag{7}$$

The transversal acceleration is f_x, the vehicle speed extracted from the odometer measurement is v_{od}, the angular rotation around the vertical Z-axis is ω_z. Besides, considering relatively low values of pitch and roll, the azimuth angle is calculated as follows:

$$\dot{A} = -\left(\omega_z - \omega_e \sin\varphi - \frac{v_e \tan\varphi}{R_N + \Omega}\right) \tag{8}$$

where R_N is the normal radius of the Earth curvature and h is the altitude. All the linear acceleration and angular rotation values are compensated for their biases and de-noised. Moreover, the three velocities can be transformed from forward velocity and computed as follow:

$$v_e = v_{od} \sin A \cos p \tag{9}$$
$$v_n = v_{od} \cos A \cos p \tag{10}$$
$$v_u = v_{od} \sin p \tag{11}$$

Considering R_M as the meridian radius of curvature, the latitude φ, the longitude λ, the altitude Ω, can be calculated as follow:

$$\dot{\varphi} = \frac{v_n}{(R_m + \Omega)} \tag{12}$$
$$\dot{\lambda} = \frac{v_e}{(R_N + \Omega)\cos\varphi} \tag{13}$$
$$\dot{\Omega} = v_u \tag{14}$$

It is worth mentioning that the primary source of error in 3D RISS is the gyroscope measurement error [14]. As its errors introduce errors in horizontal velocity and positions, which is not the case while using the accelerometers as their effects are small.

As mentioned in Section I.A, there are various techniques used in integrating the INS and GNSS. Considering the open-loop KF, in some cases, the dynamic error model is linearized around a nominal navigation state while neglecting some representative terms [24]. Also, the absence of the feedback from the KF to the INS dynamic model leads to imprecise prediction in the presence of extended GNSS outages [30].

On the other hand, the PF general INS/GNSS integration is suitable for nonlinear-based dynamic systems [27]. In PF filtering technique, extensive computational processes are held as conditional probability functions are adopted for state representation. Accordingly, particles that are weighted samples are used to approximate the probability density functions along with the prediction, update and re-sampling held at each iteration [28].

The EKF closed-loop process, as shown in Figure 1, surpasses the KF as the linearization is carried out on the corrected RISS outputs. This is besides the bias compensation of the gyroscope measurements achieved by the EKF. Thus, reliable and accurate navigation can be obtained while bypassing expensive computational processes of PF [30]. In the following paragraphs, we present the EKF 3D RISS/GNSS integration model.

For the EKF, the discrete-time domain is given by [30], [36]:

$$\delta x_{k+1} = \Phi_{k,k+1}\delta x_k + G_k w_k \Delta t \tag{15}$$

where the state transition matrix is $\Phi_{k,k+1}$, the error state vector is given by δx_k, the noise parameter matrix is G_k, w_k is a Gaussian noise vector with a zero mean and Δt is the time interval. The system dynamic matrix F can be downsized to provide the state transition matrix Φ_k. Given that the measurement model of the discrete KF is presented by [36]:

The 3D RISS error state vector is given by [30]:

$$\delta x = [\delta\varphi, \delta\lambda, \delta\Omega, \delta v_e, \delta v_n, \delta v_u, \delta A, \delta a_{od}, \delta b_z]^T \tag{16}$$

where $\delta\varphi$ is latitude error, $\delta\lambda$ is longitude error, $\delta\Omega$ is altitude error, δv_e is east velocity error, δv_n is north velocity error, δv_u is upward velocity error, δA is azimuth error, δa_{od} is the error in acceleration extracted from odometer measurements, and δb_z is the gyroscope bias error. The mentioned motion equations are linearized to obtain an error model of the closed-loop EKF used for INS/GNSS integration in this work.

This linearization process is performed by keeping only the first term of Taylor's series expansion. Accordingly, these linearized equations are used to build the $\boldsymbol{F}$ matrix, and the position of each term can be indicated by F_{mn}, where m is for the row and n is for the column. These equations are given by [30]:

$$\delta\dot{\varphi} = \underbrace{\frac{\delta v_n}{(R_M + h)}}_{F_{15}} \tag{17}$$

$$\delta\dot{\lambda} = \underbrace{\frac{\delta v_e}{(R_N + \Omega)\cos\varphi}}_{F_{24}} + \underbrace{\frac{v_e \tan\varphi}{(R_N + \Omega)\cos\varphi}}_{F_{21}} \tag{18}$$

$$\delta\dot{\Omega} = \underbrace{\delta v_u}_{F_{36}} \tag{19}$$

$$\delta\dot{v_e} = \underbrace{\sin A \cos p \delta a_{od}}_{F_{48}} + \underbrace{a_{od} \cos A \cos P}_{F_{47}}$$
$$- \underbrace{\left(\omega_z - b_z - \omega_e \sin\varphi - \frac{v_e \tan\varphi}{R_N + \Omega}\right)\delta v_n}_{F_{54}} + \underbrace{v_n}_{F_{45}}\delta b_z$$
$$+ \underbrace{v_n\left(\omega_e \cos\varphi + \frac{v_e sec^2\varphi}{R_N + \Omega}\right)\delta\varphi}_{F_{41}} + \underbrace{\frac{v_n \tan\varphi}{R_N + \Omega}\delta v_e}_{F_{44}} \tag{20}$$

$$\delta\dot{v_n} = \underbrace{\cos A \cos P}_{F_{58}}\delta a_{od} + \underbrace{a_{od}\sin A \cos P}_{F_{57}}\delta A$$
$$- \underbrace{\left(\omega_z - b_z - \omega_e \sin\varphi - \frac{2v_e \tan\varphi}{R_N + \Omega}\right)\varphi v_e}_{F_{54}} + \underbrace{v_e}_{F_{45}}\delta b_z$$
$$+ \underbrace{v_e\left(\omega_e \cos\varphi \frac{v_e sec^2\varphi}{R_N + \Omega}\right)\delta\varphi}_{F_{51}} \tag{21}$$

$$\delta\dot{v_u} = \underbrace{\sin p}_{F_{68}}\delta a_{od} \tag{22}$$

$$\delta\dot{A} = \underbrace{\delta b_z}_{F_{79}} + \underbrace{\left(\omega_e \cos\varphi + \frac{v_e sec^2\varphi}{R_N + \Omega}\right)\delta\varphi}_{F_{71}} + \underbrace{\frac{\tan\varphi}{R_N + \Omega}\delta v_e}_{F_{74}} \tag{23}$$

The odometer and gyroscope errors are modelled as a Gauss-Markov process of the first order [36] and given by:

$$\delta\dot{a_{od}} = \underbrace{\beta_{od}}_{F_{88}}\delta a_{od} + \sqrt{2\beta_{od}\sigma_{od}^2}\omega(t) \tag{24}$$

$$\delta\dot{b_z} = \underbrace{-\beta_z}_{F_{99}}\delta b_z + \sqrt{2\beta_z\sigma_z^2}\omega(t) \tag{25}$$

where β_{od} and σ_{od} are the Gauss-Markov process parameters for δa_{od}, while β_z and σ_z are for δb_z. Thus, the full dynamic $\boldsymbol{F}$ matrix can be constructed given the terms denoted at each corresponding place, and the rest of the terms are set to zero. Consequently, the measurement model for the loosely coupled integration of INS/GNSS gives the difference between the GNSS position/velocity and INS position/velocity as:

$$\delta z = \boldsymbol{D}\delta x + v \tag{26}$$

where the measurements vector δz is given by:

$$\delta z = \begin{bmatrix} \varphi_{GNSS} - \varphi_{INS} \\ \lambda_{GNSS} - \lambda_{INS} \\ h_{GNSS} - h_{INS} \\ v_{eGNSS} - v_{eINS} \\ v_{nGNSS} - v_{nINS} \\ v_{uGNSS} - v_{uINS} \end{bmatrix} \tag{27}$$

Moreover, the design matrix $\boldsymbol{D}$ is given as:

$$\boldsymbol{D} = \begin{bmatrix} 1 & 0 & 0 & 0 & 0 & 0 & 0 & 0 & 0 \\ 0 & 1 & 0 & 0 & 0 & 0 & 0 & 0 & 0 \\ 0 & 0 & 1 & 0 & 0 & 0 & 0 & 0 & 0 \\ 0 & 0 & 0 & 1 & 0 & 0 & 0 & 0 & 0 \\ 0 & 0 & 0 & 0 & 1 & 0 & 0 & 0 & 0 \\ 0 & 0 & 0 & 0 & 0 & 1 & 0 & 0 & 0 \end{bmatrix} \tag{28}$$

where the term v is a Gaussian noise vector with zero mean with covariance matrix $\boldsymbol{R} = \langle vv^T \rangle$. The EKF algorithm is divided into two stages; the prediction is given by [14]:

$$\Phi_{k,k+1} = \boldsymbol{I} + \boldsymbol{F}_k \boldsymbol{\Delta t} \tag{29}$$

$$\boldsymbol{P}_{k+1}^- = \Phi_{k,k+1}\boldsymbol{P}_k^+ \Phi_{k,k+1}^T + \boldsymbol{Q}_k \tag{30}$$

As $\boldsymbol{I}$ is the identity matrix, $\boldsymbol{P}_{k+1}^-$ is the prior estimate of error state covariance matrix and $\boldsymbol{Q}_k$ is the system noise matrix. While the update stage is given by [14]:

$$\boldsymbol{K}_{k+1} = \boldsymbol{P}_{k+1}^- \boldsymbol{D}^T \left[\boldsymbol{D}\boldsymbol{P}_{k+1}^- \boldsymbol{D}^T + \boldsymbol{R}_k \right]^{-1} \tag{31}$$

$$\delta x_{k+1}^+ = \boldsymbol{K}_{k+1}\delta z_{k+1} \tag{32}$$

$$\boldsymbol{P}_{k+1}^+ = (\boldsymbol{I} - \boldsymbol{K}_{k+1})\boldsymbol{P}_{k+1}^- \tag{33}$$

Given that, δx_{k+1}^+ is the estimation of the error state and $\boldsymbol{P}_{k+1}^+$ is the posterior error covariance matrix estimation.

In the following section, we present the capabilities of the proposed BIO 3D RISS/GNSS in providing continuous and accurate navigation solutions during different outage periods. The potential of the BIO appears in bringing up the performance of the low-cost IMUs to the high-end versions regarding the measurement quality. Also, the de-noised inertial measurements lead to accurate position computation in the mechanization process.

Furthermore, the EKF-based integration accurately predicts the navigation solution during various and extended GNSS outages that outperform the traditional KF and PF navigation solutions. The impact of the proposed BIO based de-noising appears during GNSS outages where the positioning resolution relies totally on inertial sensors. We conducted several controlled experiments where a reference solution from a high-end navigation system is available. As will be described in detail in the following section, our tests involve introducing various types of GNSS outages in terms of the motion dynamics and the periods of the interruptions. During these different GNSS outage types, we assess the performance of the BIO based de-noising method and how it can improve the positioning accuracy in challenging GNSS environment.

III. Experimental Setup, Results and Discussions

To assess the capabilities of the proposed INS/GNSS integration system, we undertook three road experiments held in Kingston, Ontario and Montreal, Quebec, spanning multiple driving scenarios and areas. During these experiments, there were periods of straight driving, taking sharp turns, driving at various speeds, and full stops. The trajectories contained downtown scenarios where the GNSS receiver experienced multipath and successive outages as well as urban roadways, highway sections, driving through a tunnel, and driving where a complete and continuous outage of GNSS was present.

The first trajectory is in downtown Kingston which includes narrow urban streets with rough road surfaces. It also involves driving at relatively low speeds. The second trajectory is in downtown Montreal which contains a dense metropolitan area with heavy traffic that requires multiple stops and starts. This trajectory has a drive in a long tunnel, which implies 220 seconds of natural GNSS outage. The third trajectory experiences highway driving at relatively high speeds between Napanee and Kingston.

In all three trajectories, the MEMS-grade IMU provided by Crossbow (model IMU300CC-100) was used as the RISS component in the proposed system. While the land vehicle forward speed was collected from the on-board diagnostics (OBD) interface using the CarChip device at a data rate of 1 Hz. The proposed system results were evaluated and compared to high-end reference solutions. In the first trajectory, the reference solution was obtained by NovAtel Span integrated solution. This solution is conducted by the integration of an OEM4 GNSS receiver with IMU-CPT logged at 100 Hz. However, the integrated solution is provided at 1 Hz.

Regarding the second and third trajectories, the reference solution is supplied by NovAtel G2 Pro-Pack SPAN unit that integrates a Honeywell HG1700 tactical-grade IMU logged at 100 Hz with an OEM4 GNSS receiver. The positioning accuracy of the two references (ground truth) is within 1.8 meters. Also, the references azimuth angle accuracy is 0.05 degrees. Further details on the specifications of the reference can be found in [37]. Regarding the specifications of the multiple IMUs used for the three trajectories, Table I summarizes their main features and specifications.

A. First Trajectory

In this trajectory, we mounted the setup on a van, as shown in Figure 3. The experiment was held in Kingston. Furthermore, as shown in Figure 4, this trajectory spans the downtown core and urban roads with different driving scenarios. These scenarios include left and right turns with different angles, straight driving, multiple stops, and various traffic conditions. The distance covered was approximately 14 kilometers, and the duration of the trajectory was approximately 35 minutes, including times when the van was stationary.

To demonstrate the BIO denoising capabilities, Figure 5. provides a sample of the inertial measurements of the low-grade IMU-Xbow before and after de-noising compared to the IMU-CPT during 35 seconds. BIO de-noising has significantly enhanced angular rotation measurements around

TABLE I
SPECIFICATIONS OF THE UTILIZED IMUS

SPECIFICATIONS	IMU300CC-100 XBOW (TRAJECTORY 1,2,3)	IMU- CPT (TRAJECTORY 1)	IMU HG1700 (TRAJECTORY 2,3)
Update Rate	>100 Hz	100 Hz	100 Hz
Gyroscopes			
Bias	$\pm 2\ deg/s$	$\pm 20\ deg/hr$	$One\ deg/hr$
Scale Factor	<1%	<0.15%	150 ppm
Angle Random Walk	$2.22\ deg/\sqrt{hr}$	$0.0667\ deg/\sqrt{hr}$	$0.125\ deg/\sqrt{hr}$
Accelerometers			
Bias	$< \pm 30\ mg$	$< \pm 50\ mg$	$1\ mg$
Scale Factor	<1%	<0.4%	300 ppm
Range	$\pm 2g$	$\pm 10g$	$\pm 50g$

Fig. 3. Testbed mounted in a land vehicle (Van) utilized for the first trajectory.

the Z-axis of the IMU-Xbow as shown in the highlighted part of Figure 5.

To assess the performance of the proposed system under GNSS complete outages, we introduced eight simulated total outages in the post-processing process. The duration of each outage is 60 seconds during various driving scenarios, speeds, and roads, as shown in Figure 4. The system performance, in Tables II and III providing the root means square (RMS) and Maximum 2D positioning error, respectively. In the two tables, we showed the errors for the 3D RISS/ GNSS and the BIO-3D RISS/GNSS systems. The BIO-3D RISS/GNSS presents better performance than 3D RISS/GNSS in terms of lower 2D positioning errors during the eight simulated outages. In conclusion, the BIO-3D RISS/GNSS enhances the average 2D RMS error of the 3D RISS/GNSS by approximately 69%.

To provide a comparison of the performance of the proposed method, we show the position solution of the BIO system
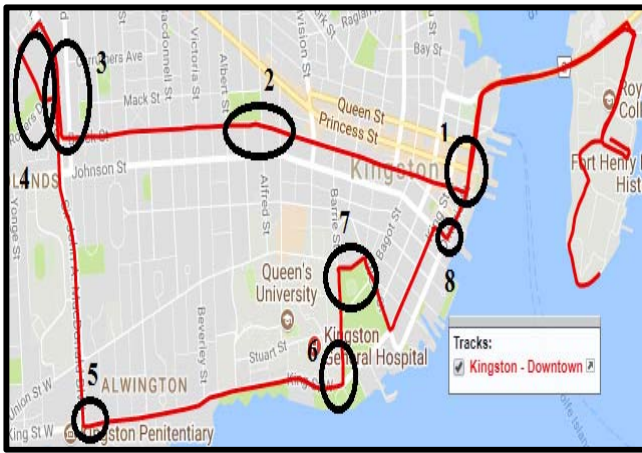
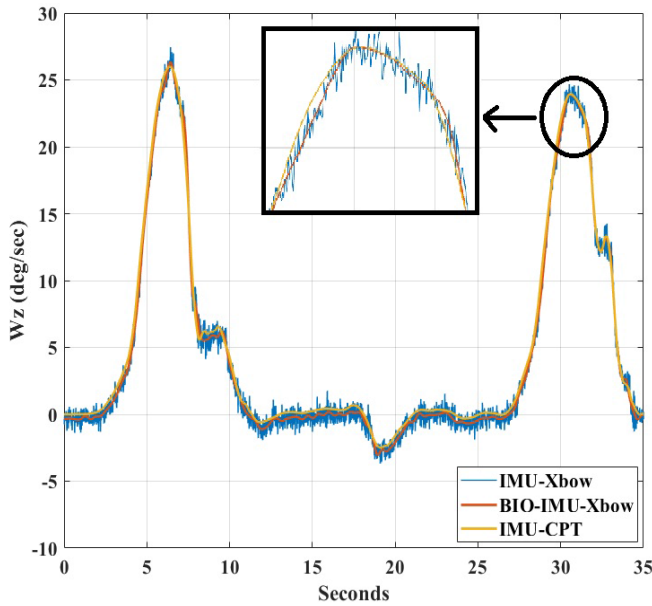Fig. 4. Road test trajectory in kingston with multiple GNSS outages (in black).

Fig. 5. Angular Rotation Measurements for the IMU-Xbow, BIO de-noised IMU-XBOW and the IMU-CPT during 35 seconds of the Frist Trajectory.

TABLE II
2D RMS HORIZONTAL POSITION ERROR IN METERS DURING GNSS OUTAGES, FIRST TRAJECTORY

OUTAGE No.	OUTAGE DURATION (SECONDS)	3D RISS/GNSS	BIO-3D RISS/GNSS
1	60	4.29	1.71
2	60	5.00	1.36
3	60	10.63	4.56
4	60	12.53	2.79
5	60	4.17	0.97
6	60	5.87	1.47
7	60	9.80	2.07
8	60	4.75	2.90
Average	60	7.13	**2.22**

along with the 3D RISS/GNSS and the NovAtel reference solutions. During the fourth outage, the land vehicle turned three times, two stop signs, and one yield sign. This route

TABLE III
2D MAXIMUM POSITION ERROR IN METERS DURING GNSS OUTAGES, FIRST TRAJECTORY

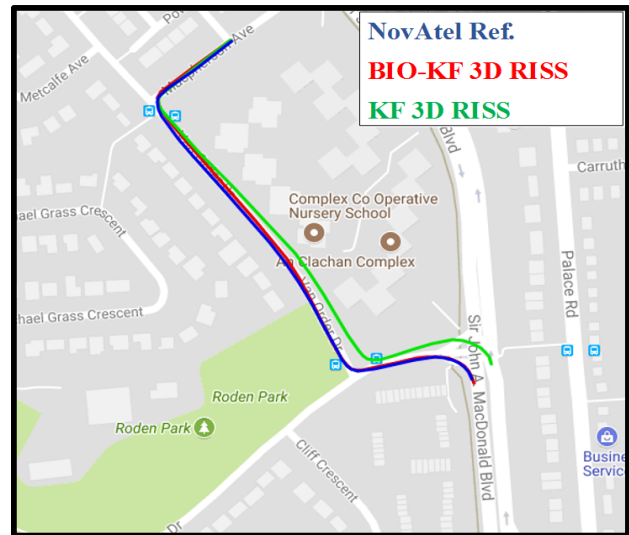| OUTAGE No.	OUTAGE DURATION (SECONDS)	3D RISS/GNSS	BIO-3D RISS/GNSS
1	60	10.75	5.53
2	60	9.23	2.52
3	60	17.68	11.59
4	60	12.53	5.77
5	60	8.08	2.92
6	60	6.48	3.96
7	60	23.13	6.86
8	60	9.43	5.26
Average	60	12.16	**5.51**

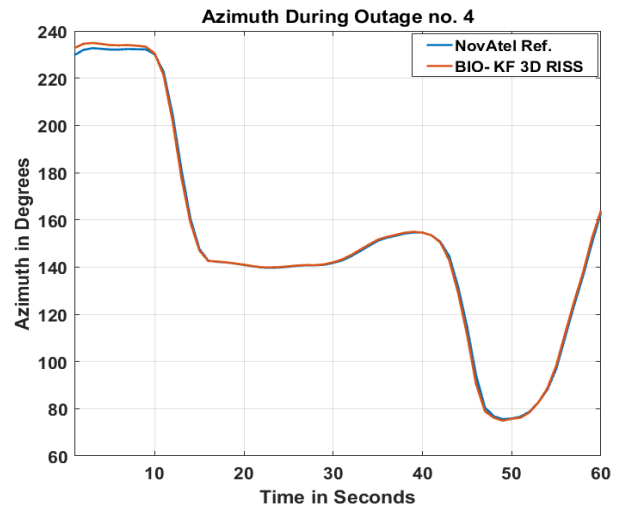Fig. 6. Positioning solution during the GNSS forth outage of the first trajectory.

Fig. 7. The azimuth of BIO-3D RISS and NovAtel reference during the forth outage of the first trajectory.

had scenarios of driving with variable speed during complete GNSS outage. The geo-referencing solutions of the two systems and the reference solution are shown in Figure 6.

In addition, Figure 7 illustrates a comparison between the azimuth angles calculated by BIO-3D RISS/GNSS system
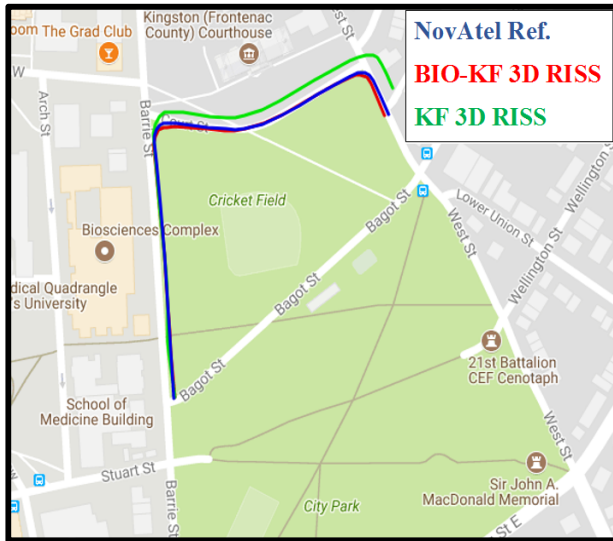
Fig. 8. Positioning solution during the GNSS seventh outage of the first trajectory.
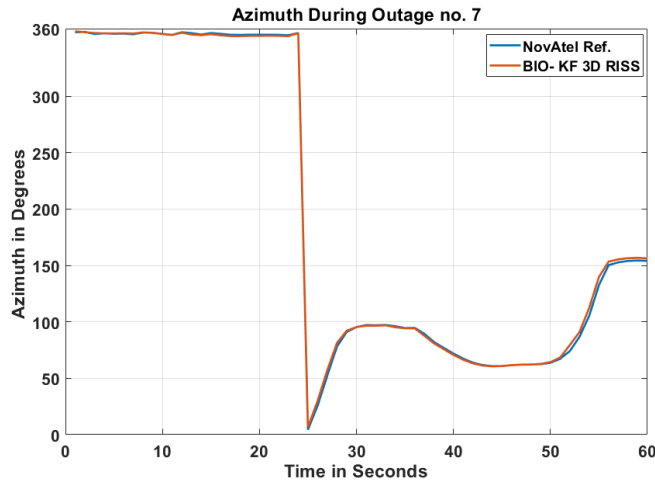

Fig. 10. Road test trajectory in montreal with multiple GNSS outages (in black).

Fig. 9. The azimuth of BIO-3D RISS and NovAtel reference during the seventh outage of the first trajectory.

TABLE IV
2D RMS HORIZONTAL POSITION ERROR IN METERS DURING GNSS OUTAGES, SECOND TRAJECTORY

OUTAGE No.	OUTAGE DURATION (SECONDS)	3D RISS/ GNSS	BIO-3D RISS/ GNSS	MPF 3D RISS
1	30	9.09	4.26	5.60
2	80	15.36	4.99	8.03
3	80	14.55	6.43	10.78
4	80	15.57	5.92	10.75
5	60	14.65	8.95	9.91
6	90	13.82	5.33	8.75
7	70	13.53	6.81	6.12
8	120	10.35	8.88	8.25
9	220	17.98	12.54	15.31
Average	92	13.87	**7.12**	9.28

and the azimuth angle extracted from NovAtel reference. The graph shows the proposed solution and how the reference coincide. We also provide the performance of the systems during the seventh outage. During this outage, the van had periods of straight driving, curvy road driving, and two right-hand turns of which one was directly after a stop sign. Figure 8. presents the navigation solution of the two systems and the reference solution. This figure shows the BIO-3D RISS/GNSS outperforms the conventional RISS/GNSS. In the seventh outage, BIO-3D RISS/GNSS has better performance than the 3D RISS/GNSS system. In Figure 9, we highlight the consistency of the azimuth calculations during outage number seven extracted from BIO-3D RISS/GNSS when compared to the NovAtel reference.

B. Second Trajectory

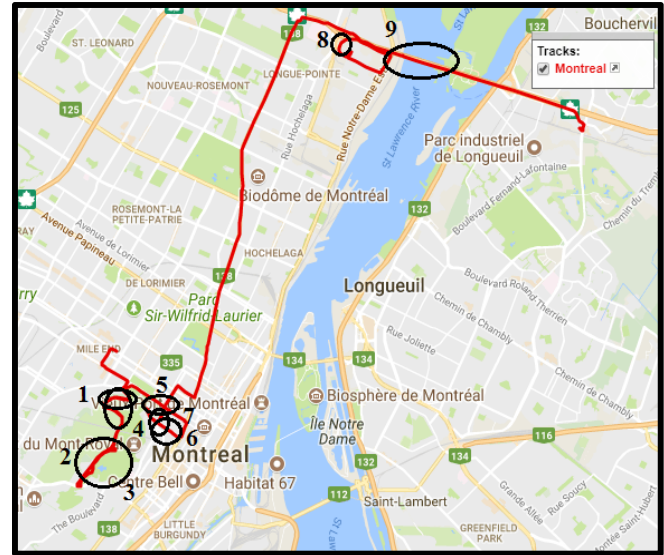For this trajectory, a van was utilized for the road experiment in Montreal. During this trajectory, a distance of approximately 100 km was covered in 85 minutes of continuous driving. As shown in Figure 10, this road test had urban roadways where some roads were straight, and some had more significant slopes. Also, the trajectory had right and left turns with various angles, multiple stops at stop signs and traffic lights, and numerous speeds according to the road nature and traffic.

To appraise the performance of the proposed system during GNSS complete outages, we introduced eight simulated outages and one real outage that occurred while driving in the tunnel crossing the St. Lawrence River. In addition to comparing the performance of the BIO-3D RISS/GNSS to the 3D RISS/ GNSS, we compared our results to the results of the MPF 3D RISS system in [27].

To ensure a fair and reliable comparison, we analyzed the results during the same outage durations and areas [27]. Accordingly, Tables IV and V present the RMS and Maximum 2D horizontal position errors for 3D RISS/ GNSS, BIO-3D RISS/ GNSS, and MPF 3D RISS concerning the same reference provided by NovAtel G2 Pro-Pack SPAN unit.

The RMS and maximum error results show a significantly better performance of the proposed system when compared

TABLE V
2D MAXIMUM HORIZONTAL POSITION ERROR IN METERS
DURING GNSS OUTAGES, SECOND TRAJECTORY

OUTAGE No.	OUTAGE DURATION (SECONDS)	3D RISS/ GNSS	BIO-3D RISS/ GNSS	MPF 3D RISS
1	30	15.34	7.44	8.30
2	80	25.80	10.83	15.98
3	80	22.31	25.26	20.81
4	80	29.84	10.25	17.80
5	60	27.29	11.89	13.82
6	90	23.76	8.41	12.96
7	70	24.16	11.86	13.86
8	120	17.02	15.65	15.29
9	220	35.56	20.85	33.41
Average	92	24.56	**13.60**	16.91

Fig. 12. The azimuth of BIO-3D RISS and NovAtel reference during the third outage of the second trajectory.

Fig. 11. Positioning solution during the GNSS third outage of the second trajectory.
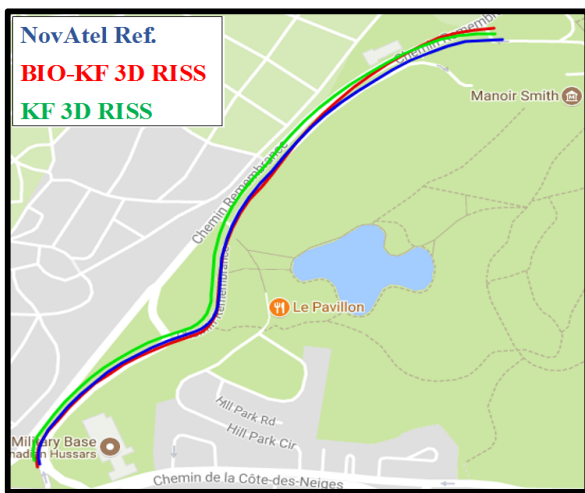

Fig. 13. Positioning solution during the GNSS forth outage of the second trajectory.

to 3D RISS/GNSS. The BIO-3D RISS/GNSS enhanced the average 2D horizontal RMS position errors by 49%. Also, enhancement of approximately 45% is achieved for the average 2D positioning maximum error. The BIO-3D RISS/GNSS outperformed the performance of MPF 3D RISS by 23%. Regarding the average 2D maximum positioning error, the proposed system surpasses the MPF 3D RISS by 20%.

These results show the significance of adopting BIO de-nosing in the closed-loop loosely coupled integration of the GNSS and INS through KF instead of applying the computationally demanding PF solutions. To give an overview of the performance of the BIO-3D RISS/GNSS system, we show the results of the positioning solutions compared to the 3D RISS/GNSS concerning the NovAtel reference solution during selected outages. A detailed description of the outages is mentioned in [27]. Also, we present the results of the azimuth angles obtained by BIO-3D RISS/ GNSS and compare it to the ones provided by the NovAtel reference for the same selected outages. In these chosen outages, we considered various driving scenarios to span multiple dynamics and areas. For the third outage, in particular, Figure 11 provides the 2D positioning solution of our system compared to 3D
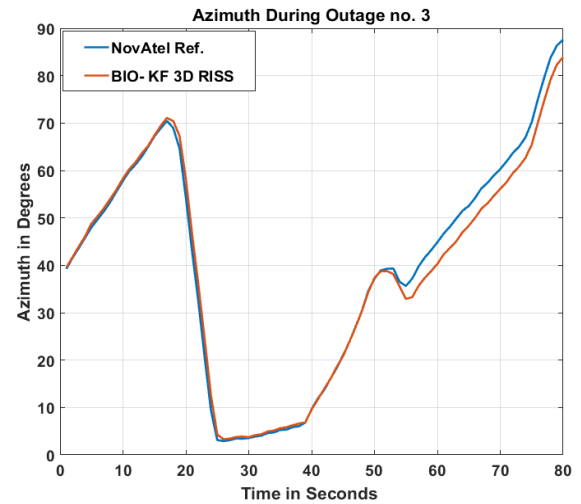
RISS/GNSS while considering a ground truth solution by the NovAtel reference. Figure 11 and Table IV shows the performance of BIO-3D RISS/GNSS regarding the average 2D position-errors.

However, towards the end of the outage, the proposed system drifts, achieving a higher maximum 2D position error compared to 3D RISS/GNSS and MPF 3D RISS. This drift affects the azimuth angle of the proposed system, as shown in Figure 12. Furthermore, we illustrate the performance of the proposed method during the forth outage in Figure 13 to examine the performance in the presence of different dynamics. Accordingly, BIO 3D RISS/GNSS grants a better positioning solution than 3D RISS/GNSS concerning the NovAtel reference solution. Moreover, we assess the system performance during the outage no.4 by comparing the azimuth angle calculated by BIO-3D RISS/GNSS with the reference, as shown in Figure 14.

Authorized licensed use limited to: Queen's University. Downloaded on May 12,2020 at 18:07:11 UTC from IEEE Xplore. Restrictions apply.

Fig. 14.   The azimuth of BIO-3D RISS and NovAtel reference during the forth outage of the second trajectory.

Fig. 15.   Positioning solution during the GNSS ninth outage of the second trajectory.

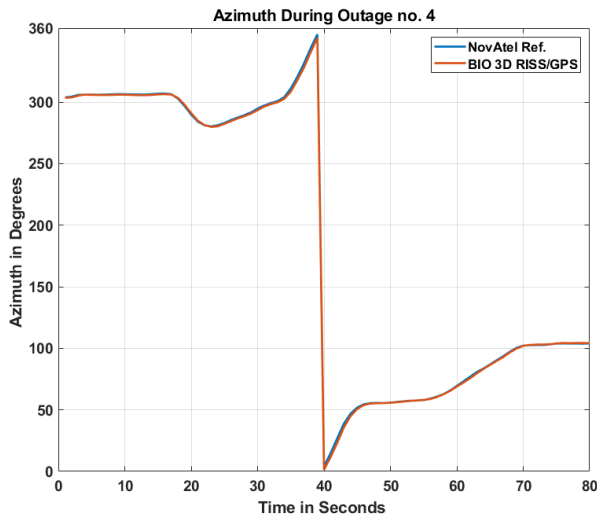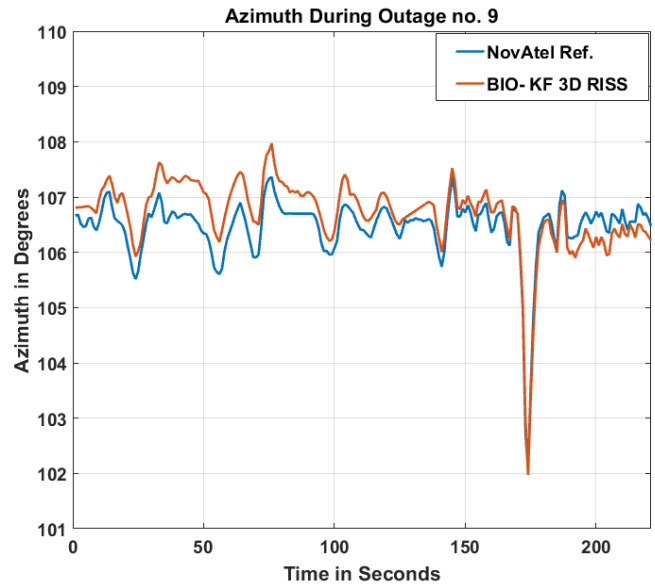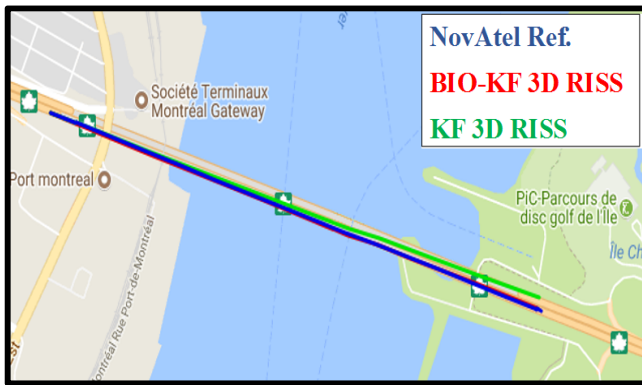Fig. 16.   The azimuth of BIO-3D RISS and NovAtel reference during the ninth outage of the second trajectory.

Fig. 17.   Road Test Trajectory between Kingston and Napanee with Multiple GNSS Outages (in black).

The azimuth of the proposed system followed the same behaviour of the azimuth extracted from the reference and provided a consistent performance through the full length of the outage. In Figure 15, we evaluate the performance of the BIO-3D RISS/GNSS system during natural and complete outages. We provide the positioning solution of the proposed method with the 3D RISS/GNSS. Both systems are compared with the reference during the ninth outage. In this outage, a complete and natural GNSS Outage occurred and lasted for 220 seconds while driving in a tunnel crossing the St. Lawrence River. The new system achieved an RMS 2D position error of 12.45 m and a maximum 2D position error of 13.60 m. These results enhanced the maximum 2D position error of 3D RISS/GNSS by 41 % and the MPF 3D RISS by nearly 38%. A consistent azimuth angle performance of the proposed system compared to the azimuth of the ground truth is shown in Figure 16.

C. Third Trajectory

The third road experiment was carried out around Kingston. The path had extended highway portions between Kingston and Napanee as well as multiple urban roadways driving.
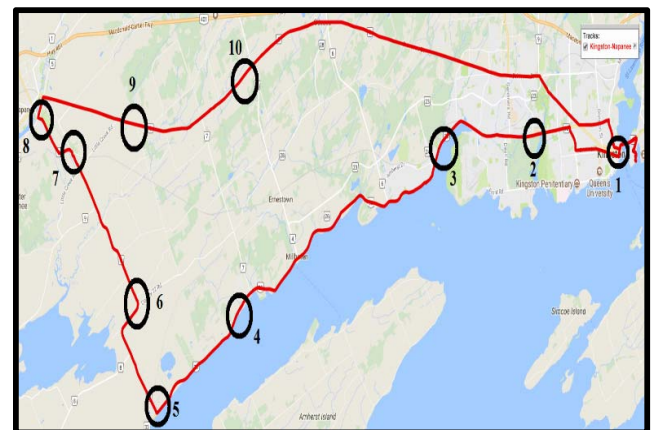
As shown in Figure 17, the experiment included various driving dynamics and areas. For analyzing the performance of the system, we introduced ten simulated GNSS outages in the same regions and durations used in [27]. These outages included different driving scenarios, speeds, and areas.

In Table VI, we present the maximum 2D position errors during the ten outages for the BIO-3D GNSS, 3D RISS/GNSS, and MPF 3D RISS concerning a positioning solution reference provided by NovAtel G2 Pro-Pack SPAN unit. The proposed system continues to have better performance compared to 3D RISS/GNSS and MPF 3D RISS. The BIO-3D RISS/GNSS provides a better average 2D maximum position error than the 3D RISS/GNSS by 62 % and outperforms the MPF 3D RISS by approximately 26 % regarding the average 2D maximum positioning errors.

To prove the capabilities of the proposed system, as an example, we extended the duration of the fifth outage to four minutes. Concerning the 2D maximum positioning errors, BIO-3D RISS/GNSS achieves a maximum error of 9.63m.

TABLE VI
2D MAXIMUM HORIZONTAL POSITION ERROR IN METERS
DURING GNSS OUTAGES, THIRD TRAJECTORY

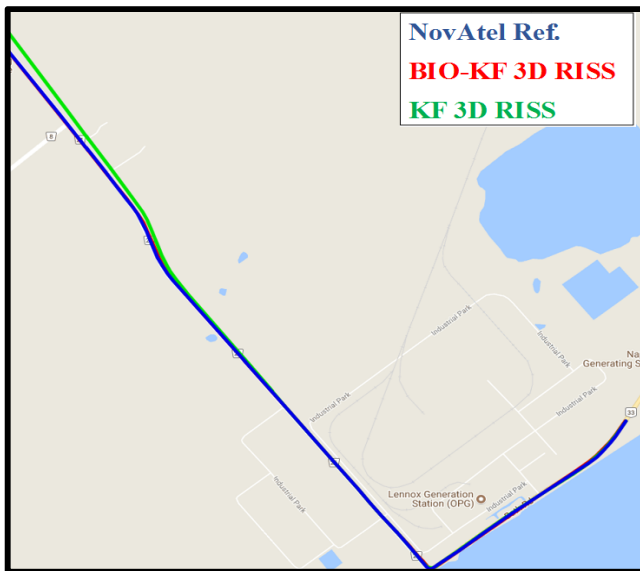| OUTAGE No.	OUTAGE DURATION (SECONDS)	3D RISS/ GNSS	BIO-3D RISS/ GNSS	MPF 3D RISS
1	60	9.69	5.94	11.53
2	60	10.55	0.99	8.25
3	60	10.87	5.27	5.49
4	60	25.33	10.09	5.44
5	60	21.63	5.36	12.53
6	60	14.04	7.8	7.52
7	60	15.81	8.88	6.05
8	60	25.04	6.02	8.24
9	60	7.82	2.29	4.46
10	60	12.17	5.53	9.74
Average	60	15.29	5.81	7.92

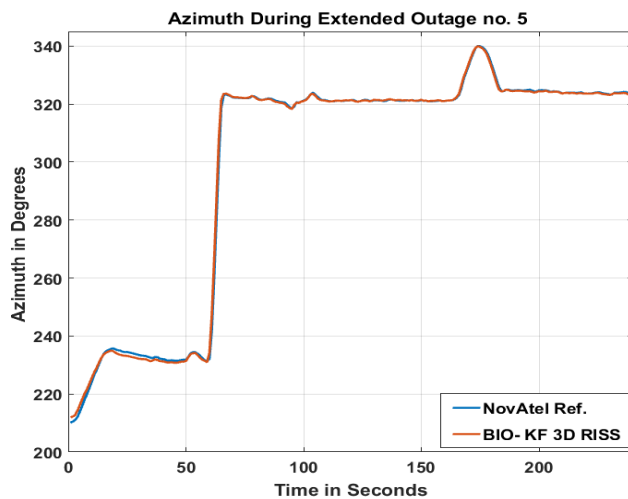Fig. 18. Positioning solution during the extended fifth GNSS outage of the third trajectory.

Fig. 19. The azimuth of BIO-3D RISS and NovAtel reference during the fifth extended outage of the third trajectory.

While the 3D RISS/GNSS mostly drifts to accomplish a 2D maximum position error of 64.70 m. To challenge the new system, as an example, we extended the duration of

TABLE VII
MATHEMATICAL SYMBOLS AND DEFINITIONS SUMMARY

MATHEMATICAL SYMBOL	DEFINITION
H	Hilbert Space
$\hat{y}$	The closest vector to y (in the minimal norm sense)
P_X	Matrix of scalars
$\{l_1, l_2, \ldots, l_k\}$	Finite set of basis
l_m	Signal representation norm-2 error
γ	Number of floating points representation
K	Number of basis elements
N	Signal length
M	Number of selected basis elements
x	Navigation state vector
φ	Latitude
λ	Longitude
Ω	Altitude
v_e	East velocity
v_n	North velocity
v_u	Upward velocity
r	Roll angle
p	Pitch angle
A	Azimuth angle
f_y	Forward acceleration
f_x	Transversal acceleration
ω_z	Angular rotation around the vertical Z-axis
g	Gravitational Acceleration
v_{od}	Odometer Speed
R_N	Normal radius of the earth curvature
R_M	Meridian radius of curvature
$\Phi_{k,k+1}$	State transition matrix
δx_k	Error state vector
G_k	Noise parameter matrix
w_k	Gaussian noise vector
Δt	Time interval
F	System Dynamic matrix
$\delta\varphi$	Latitude Error
$\delta\lambda$	Longitude Error
δv_e	East velocity error
δv_n	North velocity error
δv_u	Upward velocity error
δA	Azimuth error
$\delta a'_{od}$	Odometer error
β_{od} and σ_{od}	Gauss-Markov process parameters for odometer error
$\delta \dot{b}_z$	Gyroscope around Z-axis error
β_z and σ_z	Gauss-Markov process parameters for gyro error
δz	Measurements vector
D	Design matrix
v	Gaussian noise vector with a zero mean
R	Covariance matrix
I	Identity matrix
P_{k+1}^-	Priori estimate of error state covariance matrix
P_{k+1}^+	Posterior error covariance matrix estimation
Q_k	System noise matrix

the fifth outage to be 4 minutes, as shown in Figure 18. Concerning the 2D maximum positioning errors, BIO-3D RISS/GNSS achieves a maximum error of 9.63m. While the 3D RISS/GNSS mostly drifts to accomplish a 2D maximum position error of 64.70 m. Accordingly, Figure 19 shows the azimuth angle calculated by the proposed system and compares it to the azimuth angle obtained by the reference. The figure shows an accurate performance of BIO-3D RISS/GNSS regarding consistent azimuth angle results during complete and extended outages of GNSS. It also illustrates and proves the capabilities and reliability of the proposed method of providing accurate and continuous positioning during GNSS outages under various driving scenarios and areas.

D. Results Summary

The proposed BIO-3D RISS/GNSS positioning system has shown better performance when compared to 3D RISS/GNSS and MPF 3D RISS/GNSS positioning systems. In the first trajectory, BIO 3DRISS/GNSS achieved lower positioning errors than 3D RISS/GNSS during eight GNSS outages. These outages included different speeds, left and right turns, stop signs, road yields and traffic lights. BIO 3D RISS has enhanced the 3D RISS, 2D RMS positioning errors by 69% and 2D maximum errors by 55%.

For the second trajectory, BIO-3D RISS/ GNSS has outperformed both 3D RISS/GNSS and MPF 3D RISS/GNSS in terms of 2D RMS and 2D maximum positioning errors. The results demonstrated that BIO-3D RISS/GNSS is better in performance than the 3D RISS/GNSS in 9 GNSS outages with different duration and driving scenarios. On average, BIO-3D RISS/GNSS has enhanced the 2D RMS errors of 3D RISS/GNSS and MPF 3D RISS/GNSS by approximately 48% and 23%, respectively. Regarding the third trajectory, in 10 GNSS outages, BIO 3D RISS/GNSS has enhanced the 2D maximum positioning error of the 3D RISS/GNSS and MPF 3D RISS/GNSS by approximately 62% and 26%, respectively. During an extended outage of 4 minutes, BIO-3D RISS/GNSS has outperformed the 3D RISS/GNSS by 85% in terms of 2D maximum positioning errors. Finally, we provide Table VII to summarize all the mathematical symbols and notations, along with their corresponding definitions that are used in the paper.

IV. CONCLUSION

Considering the evolution of ITS and RIS systems, there is a high demand for accurate and continuous positioning to maintain their efficient operation in all environments. Geo-referencing road surface conditions in downtown areas relying only on GNSS technology is challenging due to satellite signal blockage and multipath effects. To offer reliable positioning integration with inertial technology is essential. This paper introduced a novel method to de-noise low-cost MEMS-based inertial sensors by using the BIO technique before processing them through inertial sensor mechanization and their integration with GNSS receivers for geo-referencing. BIO is a robust de-noising algorithm to suppress the inertial sensors' biases and noises. We were able to present an enhanced INS/GNSS integration using EKF to provide an accurate 2D position estimation during various outages in different areas and under different driving scenarios. Our system showed a 56% enhancement in geo-referencing accuracy when compared to 3D RISS/GNSS methods for three different trajectories. Compared to the MPF 3D RISS, the proposed system provided a 23% improvement in georeferencing accuracy. These results enabled providing an accurate and continuous geo-referencing during GNSS outages without adopting any additional sensors or any computational demanding integration approaches such as PF.

REFERENCES

[1] CNBC. A. Pattani. (Oct. 2016). *Building the City of the Future—At a 41 Trillion Price Tag*. [Online]. Available: https://www.cnbc.com/2016/10/25/spending-on-smart-cities-around-the-world-could-reach-41-trillion.html

[2] U. S. Department of Transportation. (Jun. 2017). *Smart City Challenge*. [Online]. Available: https://www.transportation.gov/smartcity.

[3] A. Celesti, A. Galletta, L. Carnevale, M. Fazio, A. Ĺay-Ekuakille, and M. Villari, "An IoT cloud system for traffic monitoring and vehicular accidents prevention based on mobile sensor data processing," *IEEE Sensors J.*, vol. 18, no. 12, pp. 4795–4802, Jun. 2018.

[4] Z. Xiao, P. Li, V. Havyarimana, G. M. Hassana, D. Wang, and K. Li, "GOI: A novel design for vehicle positioning and trajectory prediction under urban environments," *IEEE Sensors J.*, vol. 18, no. 13, pp. 5586–5594, Jul. 2018.

[5] H. Habizbadeh, Z. Qin, T. Soyata, and B. Kantarci, "Large-scale distributed dedicated- and non-dedicated smart city sensing systems," *IEEE Sensors J.*, vol. 17, no. 23, pp. 7649–7658, Dec. 2017.

[6] A. S. El-Wakeel et al., "iDriveSense: Dynamic route planning involving roads quality information," in *Proc. IEEE Global Commun. Conf. (GLOBECOM)*, Abu Dhabi, United Arab Emirates, Dec. 2018, pp. 1–6.

[7] J.-L. Yin, B.-H. Chen, K.-R. Lai, and Y. Li, "Automatic dangerous driving intensity analysis for advanced driver assistance systems from multimodal driving signals," *IEEE Sensors J.*, vol. 18, no. 12, pp. 4785–4794, Jun. 2018.

[8] C. Bila, F. Sivrikaya, M. A. Khan, and S. Albayrak, "Vehicles of the future: A survey of research on safety issues," *IEEE Trans. Intell. Transp. Syst.*, vol. 18, no. 5, pp. 1046–1065, May 2017.

[9] X. Wang, X. Zheng, Q. Zhang, T. Wang, and D. Shen, "Crowdsourcing in ITS: The state of the work and the networking," *IEEE Trans. Intell. Transp. Syst.*, vol. 17, no. 6, pp. 1596–1605, Jun. 2016.

[10] S. Abdelhamid, H. S. Hassanein, and G. Takahara, "Reputation-aware, trajectory-based recruitment of smart vehicles for public sensing," *IEEE Trans. Intell. Transp. Syst.*, vol. 19, no. 5, pp. 1387–1400, May 2017.

[11] R. Zhang et al., "WiFi sensing-based real-time bus tracking and arrival time prediction in urban environments," *IEEE Sensors J.*, vol. 18, no. 11, pp. 4746–4760, Jun. 2018.

[12] A. Allouch, A. Koubâa, T. Abbes, and A. Ammar, "Roadsense: Smartphone application to estimate road conditions using accelerometer and gyroscope," *IEEE Sensors J.*, vol. 17, no. 13, pp. 4231–4238, Jul. 2017.

[13] H. Xiong, J. Tang, H. Xu, W. Zhang, and Z. Du, "A robust single GPS navigation and positioning algorithm based on strong tracking filtering," *IEEE Sensors J.*, vol. 18, no. 1, pp. 290–298, Jan. 2018.

[14] A. Noureldin, T. B. Karamat, and J. Georgy, *Fundamentals of Inertial Navigation, Satellite-based Positioning and their Integration*. Berlin, Germany: Springer-Verlag, 2013.

[15] A. S. El-Wakeel et al., "Towards a practical crowdsensing system for road surface conditions monitoring," *IEEE Internet Things J.*, vol. 5, no. 6, pp. 4672–4685, Dec. 2018.

[16] S. Zhao, Y. Chen, and J. A. Farrell, "High-precision vehicle navigation in urban environments using an MEM's IMU and single-frequency GPS receiver," *IEEE Trans. Intell. Transp. Syst.*, vol. 17, no. 10, pp. 2854–2867, Oct. 2016.

[17] N. El-Sheimy, H. Hou, and X. Niu, "Analysis and modeling of inertial sensors using Allan variance," *IEEE Trans. Instrum. Meas.*, vol. 57, no. 1, pp. 140–149, Jan. 2008.

[18] A. S. El-Wakeel, A. Noureldin, N. Zorba, and H. S. Hassanein, "A framework for adaptive resolution geo-referencing in intelligent vehicular services," in *Proc. IEEE 90th Veh. Technol. Conf. (VTC-Fall)*, Honolulu, HI, USA, Sep. 2019, pp. 1–5.

[19] W. Abd-Elhamid, A. Osman, and A. Noureldin, "Wavelet multiresolution analysis for enhancing the performance of integrated GPS and MEMS-based navigation system," *Geomatica*, vol. 59, no. 1, pp. 61–72, Mar. 2005.

[20] C. W. Kang, C. H. Kang, and C. G. Park, "Wavelet De-Noising Technique for Improvement of the Low Cost MEMS-GPS Integrated System," in *Proc. Int. Symp. GPS/GNSS*, Taipei, Taiwan, Oct. 2010, pp. 26–28.

[21] A. G. Quinchia et al., "Comparison between different error modeling of MEMS applied to GPS/INS integrated systems," *Sensors*, vol. 13, no. 8, pp. 9549–9588, Jul. 2013.

[22] A. Noureldin et al., "Accuracy enhancement of inertial sensors utilizing high resolution spectral analysis," *Sensors*, vol. 12, no. 9, pp. 11638–11660, 2012.

[23] K. H. Chon, "Accurate identification of periodic oscillations buried in white or colored noise using fast orthogonal search," *IEEE Trans. Biomed. Eng.*, vol. 48, no. 6, pp. 622–629, Jun. 2001.

[24] A. Noureldin, T. B. Karamat, M. D. Eberts, and A. El-Shafie, "Performance enhancement of MEMS-based INS/GPS integration for low-cost navigation applications," *IEEE Trans. Veh. Technol.*, vol. 58, no. 3, pp. 1077–1096, Mar. 2009.

[25] J. H. Han *et al.*, "Performance analysis of two-dimensional dead reckoning based on vehicle dynamic sensors during GNSS outages," *J. Sensors*, vol. 2017, pp. 1–13, Sep. 2017.

[26] J. Georgy, A. Noureldin, M. J. Korenberg, and M. M. Bayoumi, "Modeling the stochastic drift of a MEMS-based gyroscope in gyro/odometer/GPS integrated navigation," *IEEE Trans. Intell. Transp. Syst.*, vol. 11, no. 4, pp. 856–872, Dec. 2010.

[27] J. Georgy, A. Noureldin, M. J. Korenberg, and M. M. Bayoumi, "Low-cost three-dimensional navigation solution for RISS/GPS integration using mixture particle filter," *IEEE Trans. Veh. Technol*, vol. 59, no. 2, pp. 599–615, Feb. 2010.

[28] P. Aggarwal, Z. Syed, and N. El-Sheimy, "Hybrid extended particle filter (HEPF) for integrated civilian navigation system," in *Proc. IEEE/ION PLANS*, Monterey, CA, USA, May 2008, pp. 984–992.

[29] I. Skog and P. Handel, "In-car positioning and navigation A survey," *IEEE Trans. Intell. Transp. Syst.*, vol. 10, no. 1, pp. 4–21, Mar. 2009.

[30] T. B. Karamat, M. M. Atia, and A. Noureldin, "An enhanced error model for EKF-based tightly-coupled integration of GPS and land vehicle's motion sensors," *Sensors*, vol. 15, no. 9, p. 24269, 2015.

[31] T. Genossar and M. Porat, "Optimal bi-orthonormal approximation of signals," *IEEE Trans. Syst., Man, Cybern. Syst.*, vol. 22, no. 3, pp. 449–460, May/Jun. 1992.

[32] W. W. Hager, "Updating the inverse of a matrix," *SIAM Rev.*, vol. 31, no. 2, pp. 221–239, Jun. 1989.

[33] R. Hunger, "Floating point operations in matrix-vector calculus," Munich Univ. Technol., München, Germany, Tech. Rep. TUM-LNS-TR-05-05, Oct. 2005.

[34] U. Iqbal *et al.*, "Enhancing Kalman filtering-based tightly coupled navigation solution through remedial estimates for pseudo-range measurement using parallel cascade identification," *Instrum. Sci. Technol.*, vol. 40, pp. 530–566, Jul. 2012.

[35] A. Noureldin, D. Irvine-Halliday, and M. P. Mintchev, "Accuracy limitations of FOG-based continuous measurement-while-drilling surveying instruments for horizontal wells," *IEEE Trans. Instrum. Meas.*, vol. 51, no. 6, pp. 1177–1191, Dec. 2002.

[36] T. B. Karamat, R. G. Lins, S. N. Givigi, and A. Noureldin, "Novel EKF-based vision/inertial system integration for improved navigation," *IEEE Trans. Instrum. Meas.*, vol. 67, no. 1, pp. 116–125, Jan. 2017.

[37] USER MANUAL NovAtel. *SPANTM Technology System*. Accessed, Dec. 2019. [Online]. Available: https://www.novatel.com/assets/Documents/Manuals/om-20000062.pdf

Abdalla Osman received the Ph.D. degree in geomatics engineering from the University of Calgary, Calgary, Canada, in 2010. He is currently a Research Associate with the Department of Electrical and Computer Engineering, Royal Military College of Canada. His research interests include underwater acoustics, signal processing, positioning, and navigation.

Nizar Zorba (S'02–M'08–SM'18) received the B.Sc. degree in electrical engineering from JUST University, Jordan, in 2002, the M.Sc. degree in data communications and the M.B.A. degree from the University of Zaragoza, Zaragoza, Spain, in 2004 and 2005, respectively, and the Ph.D. degree in signal processing for communications from UPC Barcelona, Spain, in 2007.

He is a Professor with the Electrical Engineering Department, Qatar University. He has more than 115 publications in journals and conference proceedings and his work led to five patents. His research interests span 5G networks optimization, demand-response in smart grids, and crowd management.

Dr. Zorba is currently the Vice-Chair of the IEEE ComSoc Communication Systems Integration and Modeling Technical Committee.

Hossam S. Hassanein (S'86–M'90–SM'05–F'17) received the Ph.D. degree in computing science from the University of Alberta, Edmonton, AB, Canada, in 1990.

He is a leading authority in the areas of broadband, wireless and mobile networks architecture, protocols, control, and performance evaluation. His record spans more than 500 publications in journals, conferences, and book chapters, in addition to numerous keynotes and plenary talks at flagship venues. He is also the Founder and the Director of the Telecommunications Research Lab, School of Computing, Queen's University, Kingston, ON, Canada, with extensive international academic and industrial collaborations.

Dr. Hassanein was a recipient of several recognitions and best paper awards at top international conferences and has led a number of symposia in flagship ComSoc conferences. He is the past Chair of the IEEE Communication Society Technical Committee on Ad hoc and Sensor Networks. He is the IEEE Communications Society Distinguished Speaker (Distinguished Lecturer, from 2008 to 2010).

Amr S. El-Wakeel (S'08) received the B.Sc. (Hons.) and M.Sc. degrees in electrical and communication engineering from the Arab Academy for Science and Technology (AAST), Cairo, Egypt, in 2008 and 2013, respectively. He is currently pursuing the Ph.D. degree in electrical and computer engineering with Queen's University, Kingston, ON, Canada.

He is also a Research Assistant with the NavINST & TRL Research Labs, Queen's University. His research work appeared in IEEE flagship conferences and top tier journals. His research interests span signal processing and machine learning to the applications of the Internet of Things and the connected and autonomous vehicles.

Mr. El-Wakeel is a member of the IEEE ComSoc and VTS. He also serves as a TPC member of the IEEE flagship conferences and a Reviewer for the IEEE, Elsevier, Springer, OSA, and Wiley journals. He received the Second Prize of the IEEE ComSoc Student Competition 2018 and the Graduate Research Award of the IEEE Kingston Section in 2019. He was a recipient of the Best Paper Award of the IEEE International Wireless Communications and Mobile Computing (IWCMC) Conference 2018.

Aboelmagd Noureldin (S'98–M'02–SM'08) received the B.Sc. degree in electrical engineering and the M.Sc. degree in engineering physics from Cairo University, Egypt, in 1993 and 1997, respectively, and the Ph.D. degree in electrical and computer engineering from the University of Calgary, AB, Canada, in 2002.

He is a Professor with the Department of Electrical and Computer Engineering, Royal Military College of Canada (RMCC), and a Cross-Appointment with the School of Computing and the Department of Electrical and Computer Engineering, Queen's University. He is an adjunct with the Department of Mathematics and Engineering Physics, Cairo University, Egypt. He is also the Founder and the Director of the Navigation and Instrumentation Research Lab, RMCC/Queen's University. His research is related to GPS, wireless location and navigation, indoor positioning, and multi-sensor fusion. He has published over 230 articles in journals and conference proceedings. His research work led to ten patents in the area of position, location, and navigation systems.